Elastic Vector Solitons in Soft Architected Materials

B. Deng,[1] J. R. Raney,[2] V. Tournat,[1,3] and K. Bertoldi[1,4]

[1]*Harvard John A. Paulson School of Engineering and Applied Sciences, Harvard University,
Cambridge, Massachusetts 02138, USA*
[2]*Department of Mechanical Engineering and Applied Mechanics, University of Pennsylvania,
Philadelphia, Pennsylvania 19104, USA*
[3]*LAUM, CNRS, Université du Maine, Avenue Olivier Messiaen, 72085 Le Mans, France*
[4]*Kavli Institute, Harvard University, Cambridge, Massachusetts 02138, USA*

We demonstrate experimentally, numerically, and analytically that soft architected materials can support the propagation of elastic vector solitons. More specifically, we focus on structures comprising a network of squares connected by thin and highly deformable ligaments and investigate the propagation of planar nonlinear elastic waves. We find that for sufficiently large amplitudes two components—one translational and one rotational—are coupled together and copropagate without dispersion. Our results not only show that soft architected materials offer a new and rich platform to study the propagation of nonlinear waves, but also open avenues for the design of a new generation of smart systems that take advantage of nonlinearities to control and manipulate the propagation of large amplitude vibrations.

Highly deformable, soft structures characterized by a nonlinear response have enabled the design of new classes of tunable and responsive systems and devices, including soft robots [1,2], self-regulating microfluidics [3], reusable energy absorbing systems [4,5], and materials with programable response [6]. Furthermore, soft architected materials (also referred to as soft or nonlinear metamaterials) present opportunities to control the propagation of elastic waves, since their dispersion properties can be altered by applying a large, nonlinear predeformation [7–9]. However, most of the investigations have exclusively focused on linear stress waves, although the compliant nature of soft systems is capable of supporting large-amplitude nonlinear waves.

Nonlinear waves not only display a very rich behavior, but also enable a broad range of applications, including impact mitigation layers [10,11], asymmetric transmission [12,13], switches [14], and lenses [15]. While such waves have mostly been studied in granular media [10–16], soft architected materials also provide an ideal environment for their propagation. In fact, even soft metamaterials made of a single linear material can support a wide range of effective nonlinear behaviors that are determined by the architecture. This marks an important difference between soft architected materials and granular media, since in the latter the nonlinear response is determined by the contacts between grains, and those are difficult to control [17], especially in 2D.

In this Letter, we combine analytical, numerical, and experimental tools to study the propagation of large-amplitude nonlinear waves in a structure comprising a network of squares connected by thin and highly deformable ligaments. While the behavior of this system under quasistatic loading has attracted significant interest as it is characterized by an effective negative Poisson ratio

[18–20], here we focus on its dynamic response and demonstrate how the geometry of the system directly affects its nonlinear dynamic elastic properties. We investigate the propagation of nonlinear waves of mixed translational and rotational nature and demonstrate the existence of vector elastic solitons. Moreover, we show that by tuning the geometry of the structure a wide range of dispersive and nonlinear dynamic properties can be achieved.

Our system consists of a network of square domains connected by thin ligaments (see Fig. 1), all made of elastomeric material [polydimethylsiloxane (PDMS)]. The squares have edge lengths of approximately 8 mm and diagonals of length $2l \approx 11.3$ mm that are rotated by an angle $\theta_0 = 25°$ with respect to the horizontal and vertical directions [see Fig. 1(a)]. A system comprising 6×40 squares is fabricated with high fidelity using direct ink writing, an extrusion-based 3D printing method [21,22] [see Supplemental Material (SM) for details [23]]. After printing, all squares are filled with PDMS and a small copper cylinder with radius 2.38 mm is also placed at their center in order to modify the medium inertial properties.

We start by investigating experimentally the propagation of pulse waves in the system. Impact experiments are conducted in which a custom aluminum impactor is used to initiate simultaneous rotation and displacement of the squares at one end of the sample [see Fig. 1(a) and Movies S1 and S2 in SM [23]]. Different displacement signals are applied to the first column of square by varying both the initial gap between the impactor and the structure (defining the maximum imposed displacement) and the strength of the pulse applied to the impactor (mostly influencing the maximum imposed velocity). The propagation of the resulting pulses through the entire sample is
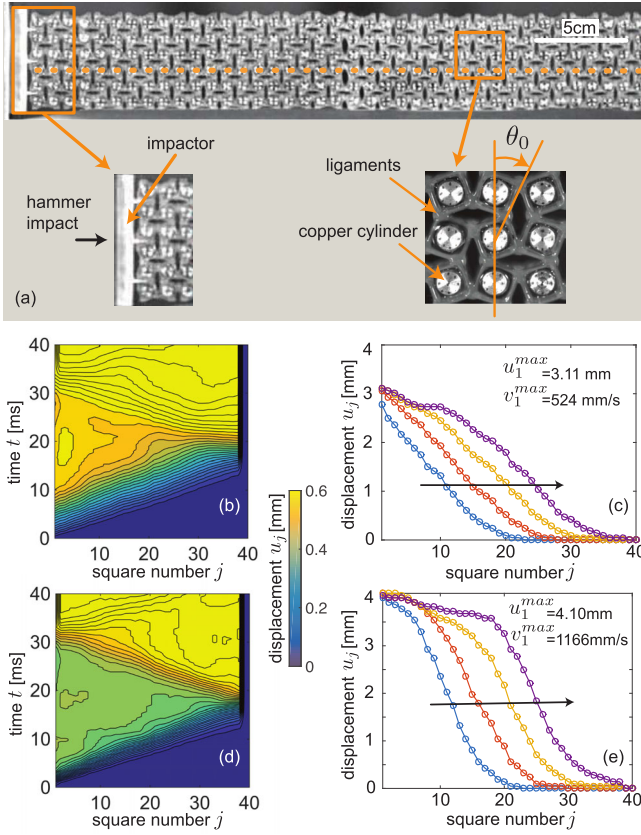
FIG. 1. (a) The system consists of a network of square domains connected by thin ligaments. Pulse waves are generated by a hammer strike on an aluminium impactor and propagate from left to right. (b)–(d) Spatiotemporal displacement diagrams and (c)–(e) spatial displacement profiles at $t = 7, 10, 13, 16$ ms for an impact characterized by (b),(c) $(u_1^{max}, v_1^{max}) = (3.11 \text{ mm}, 524 \text{ mm/s})$ and (d),(e) $(u_1^{max}, v_1^{max}) = (4.10 \text{ mm}, 1166 \text{ mm/s})$.

observed using a high-speed camera (Photron FASTCAM SA1) recording at 3000 Hz. The horizontal displacement u_j of the jth square located in the third row [highlighted by a horizontal orange line in Fig. 1(a)] is then obtained by tracking the marker positioned at its center with a digital image correlation analysis [25].

In Figs. 1(b)–1(e) we show results for two experiments in which the impactor prescribes a displacement signal to the first square characterized by $(u_1^{max}, v_1^{max}) = (\max(u_1), \max(v_1)) = (3.11 \text{ mm}, 524 \text{ mm/s})$ and $(u_1^{max}, v_1^{max}) = (4.10 \text{ mm}, 1166 \text{ mm/s})$ (v_1 denoting the velocity of the first square), respectively. Note that the input displacement and velocity profiles [i.e., $u_1(t)$ and $v_1(t)$] are shown in Fig. S2 of SM [23]. The evolution of the horizontal displacements u_j indicates that there is a pulse propagating through the sample that is reflected a couple of times by the boundaries before vanishing [Figs. 1(b) and 1(d)]. Moreover, by comparing the displacement u_j of all squares at different times [Figs. 1(c) and 1(e)], we find that the pulses conserve their spatial shape during propagation, suggesting that the system can support

the propagation of solitary waves. The experimental movies also reveal that the squares not only move horizontally when the pulse propagates, but also rotate (see Movies S1, S2, and S3 of SM [23]). However, the image resolution (about 20 pixels per square edge length) is not enough to monitor with sufficient accuracy their rotation. To capture the rotational waves propagating through the sample, we conduct an additional set of experiments where the camera is focused only on four squares, located at two-thirds of the sample. The results reported in Fig. S1 and Movie S3 of SM [23] clearly confirm the simultaneous propagation of translational and rotational waves in our structure.

To get a better understanding of the dynamic response of the structure, we investigate its behavior both numerically and analytically. Since our experiments indicate that, when the pulse propagates, the squares remain rigid and the deformation localizes at the hinges, we introduce a discrete model composed of periodically arranged rigid squares connected by linear springs at their vertices [see Fig. 2(a)]. More specifically, since the applied deformation is found to induce both translation and rotation of the squares [18–20], we consider two linear springs at each vertex, a compression or tension spring with stiffness k and a torsional spring with stiffness k_θ. Moreover, since we only consider the propagation of planar waves in the x direction, guided by our experiments we assign two degrees of freedom to the jth rigid square: the displacement in the x direction u_j and the rotation θ_j [see Fig. 2(a)]. Note that, as indicated by the blue and red arrows in Fig. 2(a), we define the positive direction of rotation alternatively for neighboring squares [i.e., if for the jth square a clockwise rotation is positive, then for the $(j-1)$th and $(j+1)$th ones counterclockwise rotation is considered as positive].

Assuming periodic boundary conditions in the y direction, it follows that the governing equations of motion for the jth square can be written as (see SM for details [23])

$$m \frac{\partial^2 u_j}{\partial t^2} = k[u_{j+1} - 2u_j + u_{j-1}$$
$$- l\cos(\theta_{j+1} + \theta_0) + l\cos(\theta_{j-1} + \theta_0)]$$
$$+ \frac{k_\theta}{l}(\theta_{j+1} - \theta_{j-1})\sin(\theta_j + \theta_0), \quad (1)$$

$$J \frac{\partial^2 \theta_j}{\partial t^2} = -k_\theta(\theta_{j+1} + 6\theta_j + \theta_{j-1})$$
$$- kl(u_{j+1} - u_{j-1})\sin(\theta_j + \theta_0)$$
$$+ kl^2\cos(\theta_j + \theta_0)[\sin(\theta_{j+1} + \theta_0)$$
$$+ \sin(\theta_{j-1} + \theta_0) - 2\sin(\theta_j + \theta_0)]$$
$$+ kl^2\sin(\theta_j + \theta_0)[\cos(\theta_{j+1} + \theta_0) + 6\cos(\theta_j + \theta_0)$$
$$+ \cos(\theta_{j-1} + \theta_0) - 8\cos(\theta_0)], \quad (2)$$

where m and J denote the mass and the moment of inertia of the squares, respectively. For the structure considered in
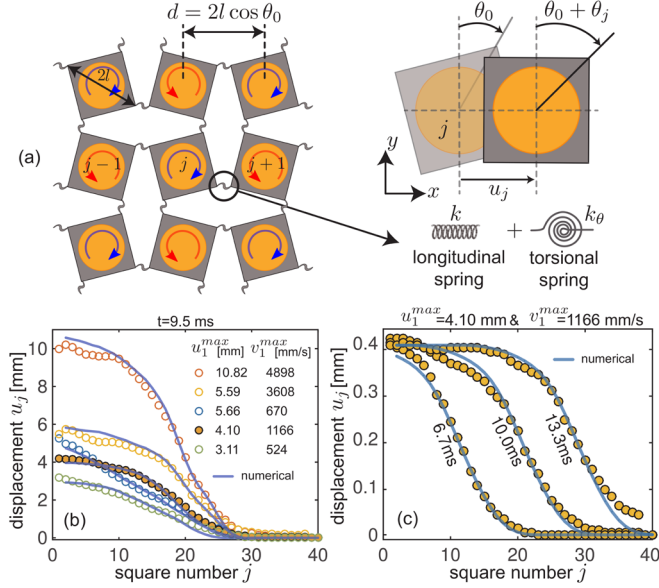
FIG. 2. (a) Schematics of the system. (b) Spatial displacement profiles at time $t = 9.5$ ms for five different impacts characterized by different combinations of u_1^{max} and v_1^{max}. (c) Spatial displacement profiles at $t = 6.7$, 10 at 13.3 ms for a single experiment with $(u_1^{max}, v_1^{max}) = (4.10$ mm, 1166 mm/s). In (b) and (c) both experimental results (markers) and numerical prediction (blue lines) are shown.

this study, we have $m = 2.093$ g and $J = 18.11$ g mm^2. Moreover, the stiffnesses k and k_θ can be estimated from the experimentally measured maximal group velocity and numerically calculated stiffness under uniaxial compression, respectively (see SM for details [23]), yielding $k = 19235$ N/m and $k_\theta = 0.0427$ Nm/rad. Finally, we note that in this model we neglect the effect of damping, which is known to have a pronounced effect on the dynamic response of structures made of soft materials. This is because here we focus on waves propagating for a relatively short distance (before reflection at the right boundary). In this case we find that damping reduces the displacement amplitude by less than 10% and does not alter the studied nonlinear effects.

To test the relevance of our discrete model, we numerically solve Eqs. (1) and (2) using the Runge-Kutta method and compare their predictions to our experimental results. In our numerical analysis we consider a chain comprising 40 squares, apply the experimentally extracted displacement signal $u_1(t)$ to the first square on the left [while fixing its rotation, i.e., $\theta_1(t) = 0$], and implement free-boundary conditions at the right end. In Fig. 2(b) we report numerical and experimental results at $t = 9.5$ ms for different impact conditions, while in Fig. 2(c) we focus on an impact for which $u_1^{max} = 4.10$ mm and $v_1^{max} = 1166$ mm/s and compare the numerical predictions and experimental data at different times. Both plots show that the pulse profiles and amplitudes are well captured by the discrete model. Moreover, the numerical results in Fig. 2(c) confirm that

for certain impact conditions the pulse propagates with no apparent distortion.

While Eqs. (1) and (2) contain the full nonlinear and dispersive terms of the modeled system, a deeper insight into its dynamics can be achieved by further simplifying them to derive analytical solutions. To this end, we first introduce the normalized displacement $U_j = u_j/2l\cos(\theta_0)$, time $T = t\sqrt{k/m}$, stiffness $K = k_\theta/kl^2$, and inertia $\alpha = l/(\sqrt{J/m})$ (see SM for details [23]). Second, we take the continuum limit of Eqs. (1) and (2) and retain the nonlinear terms up to second order, as well as the dominant dispersion terms, obtaining (see SM for details [23])

$$\frac{\partial^2 U}{\partial T^2} = \frac{\partial^2 U}{\partial X^2} + (1 - K)\tan(\theta_0)\frac{\partial \theta}{\partial X}, \tag{3}$$

$$\frac{\partial^2 \theta}{\partial T^2} = \alpha^2 \left\{ [\cos(2\theta_0) - K]\frac{\partial^2 \theta}{\partial X^2} - 2\sin(2\theta_0)\frac{\partial U}{\partial X} \right.$$
$$- 4\left[2K + \cos^2(\theta_0)\frac{\partial U}{\partial X} + 2\sin^2(\theta_0)\right]\theta$$
$$\left. - 4\sin(2\theta_0)\theta^2 \right\}, \tag{4}$$

where $X = x/2l\cos(\theta_0)$, with x denoting the coordinate along the x axis. Finally, we introduce the traveling wave coordinate $\zeta = X - cT$, c being the normalized pulse velocity, so that Eqs. (3) and (4) become

$$\frac{\partial^2 U}{\partial \zeta^2} = -\frac{(1 - K)\tan(\theta_0)}{1 - c^2}\frac{\partial \theta}{\partial \zeta}, \tag{5}$$

$$\frac{\partial^2 \theta}{\partial \zeta^2} = 2\alpha^2\beta\sin(2\theta_0)\frac{\partial U}{\partial \zeta} + 4\alpha^2\beta\sin(2\theta_0)\theta^2$$
$$+ 4\alpha^2\beta\left[2K + \cos^2(\theta_0)\frac{\partial U}{\partial \zeta} + 2\sin^2(\theta_0)\right]\theta, \tag{6}$$

where $\beta = [\alpha^2(\cos(2\theta_0) - K) - c^2]^{-1}$. Note that the displacement $U(\zeta, T)$ and rotation $\theta(\zeta, T)$ are now continuous functions of ζ and T. By integrating Eq. (5) with respect to ζ and assuming a zero integration constant (i.e., a wave with a finite temporal support), we obtain

$$\frac{\partial U}{\partial \zeta} = -\frac{(1 - K)\tan(\theta_0)}{(1 - c^2)}\theta, \tag{7}$$

which can then be substituted into Eq. (6) to obtain

$$\frac{\partial^2 \theta}{\partial \zeta^2} + P\theta + Q\theta^2 = 0, \tag{8}$$

where

$$P = \frac{4\alpha^2\beta}{(1 - c^2)}[(2c^2 - 1 - K)\sin^2\theta_0 - 2(1 - c^2)K],$$

$$Q = \frac{2\alpha^2\beta}{(1 - c^2)}(2c^2 - 1 - K)\sin(2\theta_0).$$

Note that Eq. (8) has the form of the well-known nonlinear Klein-Gordon equation with quadratic nonlinearity [26]. When $P < 0$ and $Q > 0$, analytical solutions of Eq. (8) exist in the form of a solitary wave with a stable profile,

$$\theta = A \text{sech}^2 \frac{\zeta}{W}, \tag{9}$$

where A is the amplitude of the pulse and c and W are its velocity and characteristic width, which can be determined as (see SM for details [23])

$$c = \sqrt{\frac{6K + 3(1+K)\sin^2(\theta_0) + A(1+K)\sin(2\theta_0)}{6K + 6\sin^2(\theta_0) + 2A\sin(2\theta_0)}},$$

$$W = \frac{1}{\alpha}\sqrt{\frac{(1-c^2)[\alpha^2(\cos(2\theta_0)-K)-c^2]}{2(1-c^2)K + (1-2c^2+K)\sin^2(\theta_0)}}. \tag{10}$$

Finally, by substituting Eq. (9) into Eq. (7), the solution for the displacement is found as

$$U = A\frac{(1-K)W\tan(\theta_0)}{(1-c^2)}\left(1 - \tanh\frac{\zeta}{W}\right). \tag{11}$$

Equations (9) and (11) reveal a unique feature of our system: its ability to support an elastic vector soliton. In fact, in our nonlinear system two components—one translational and one rotational—are coupled together and copropagate without distortion nor splitting. While vector solitons have been previously observed in optics [27,28], this is the first time—to the best of our knowledge—that such a phenomenon is experimentally observed in the elastic case. Finally, we note that even in the linear regime our system supports coupled translational-rotational modes (see SM for details [23]), a feature previously only observed in granular crystals [29,30].

Next, we test the validity of our analytical solution Eqs. (9)–(11) by comparing it to numerical results obtained by direct integration of the full discrete model [Eqs. (1) and (2)]. Note that in this set of simulations we assign to the first square on the left the displacement and rotation signals given by Eqs. (9) and (11), respectively, and keep free-boundary conditions at the right end. In Fig. 3(a) we focus on the structure considered in this study (for which $\theta_0 = 25°$, $\alpha = 1.7$, and $K = 0.073$) and show the profiles predicted analytically and numerically for both displacement (left axis) and rotation (right axis) assuming $A = 0.05$. We find an excellent agreement between our analytical (lines) and numerical (markers) results. While for this set of parameters our theory predicts the propagation of a solitary wave with velocity $c = 0.8152$ and characteristic width $W = 5.9071$, the numerical simulations show the propagation of a pulse that conserves its spatial shapes and is characterized by $c \sim 0.8030$ and $W \sim 5.8824$. It is important to note that, as shown by Eq. (10), both the pulse width and velocity can be tuned and controlled by
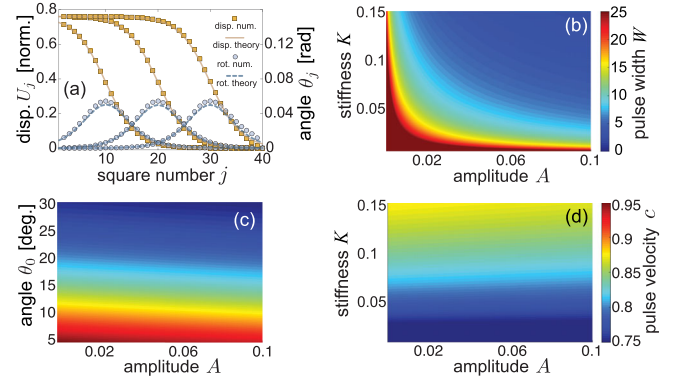
FIG. 3. (a) Comparison between analytically (lines) and numerically (markers) predicted normalized displacement and rotation profiles at $T = 10$, 20, and 30 and for $\theta_0 = 25°$, $\alpha = 1.7$, $K = 0.073$. (b) Evolution of W as a function of A and K (assuming $\theta_0 = 25°$ and $\alpha = 1.7$). (c) Evolution of c as a function of A and θ_0 (assuming $K = 0.073$ and $\alpha = 1.7$). (d) Evolution of c as a function of A and K (assuming $\theta_0 = 25°$ and $\alpha = 1.7$).

altering either the amplitude of the wave (i.e., by changing A) or the geometry of the structure (i.e., by changing θ_0, K, and α). To highlight this important point, in Figs. 3(b)–3(d) we report the evolution of c and W as a function of A, K, and θ_0. The contour plots indicate that W can be tuned by varying either A or K. Differently, we find that c is affected by changes in θ_0 and K (see also Fig. S5 of SM [23]). The plots also reveal another interesting feature of our system: the solitons propagate faster for smaller amplitudes.

Finally, in Fig. 4 we compare the analytical solution to our experimental results. More specifically, for each experiment we extract the maximum displacement and velocity experienced by the 1st, 2nd, 5th, 10th, 15th, and 20th squares and report them together with the analytical prediction (purple line) in the $U^{\max}$-$V^{\max}$ plane [where $U^{\max} = \max(U)$ and $V^{\max} = \max(dU/dT)$]. Interestingly, we find that all applied excitations result in the propagation of a soliton. If the input is close to a soliton solution, the pulse is immediately stable (i.e., even for square number < 5 the experimental markers are close to the analytical curve). In contrast, if the applied impact results in a displacement signal far from that of the supported solitary wave, it takes 10–20 squares for the wave to become stable. However, it is important to note that this observation is not general and relates to the limited variety of excited displacement profiles (all of them are reasonably close to tanh; see Fig. S2 of SM [23]). Finally, in all experiments we find a slight displacement amplitude decrease along propagation, most probably the signature of the intrinsic material damping.

In summary, we have studied experimentally, numerically, and analytically the propagation of large-amplitude nonlinear elastic waves in a structure comprising a network of squares connected by thin and highly deformable ligaments. Our results indicate that the system supports

PHYSICAL REVIEW LETTERS
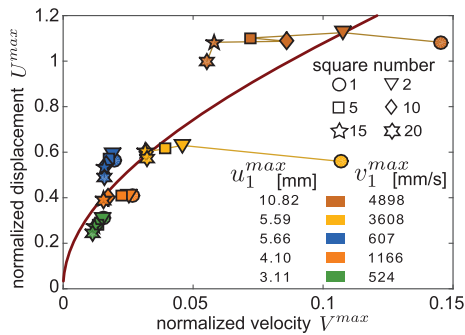
FIG. 4. Comparison between analytical solution (continuous line) and experimental results (markers). Experimental results are reported for five different impacts characterized by different combinations of u_1^{max} and v_1^{max}.

vector elastic solitons (i.e., stable nonlinear waves with two coupled components—one translational and one rotational), whose properties can be controlled by tuning the geometry of the structure. While in this study we focused on the propagation of planar waves in an homogeneous soft architected material, the response of such systems is very rich and there remains much to be investigated: How do nonplanar waves propagate in 2D soft architected materials? How do inhomogeneities and defects affect the propagation of the solitons? Can the system support bright or dark solitons? Can we excite topological solitons? We believe that the tools proposed in this study will help in answering all these questions and, ultimately, in designing a new class of structures and devices capable of controlling high amplitude waves and vibrations.

[1] R. F. Shepherd, F. Ilievski, W. Choi, S. A. Morin, A. A. Stokes, A. D. Mazzeo, X. Chen, M. Wang, and G. M. Whitesides, Proc. Natl. Acad. Sci. U.S.A. **108**, 20400 (2011).

[2] D. Yang, B. Mosadegh, A. Ainla, B. Lee, F. Khashai, Z. Suo, K. Bertoldi, and G. M. Whitesides, Adv. Mater. **27**, 6323 (2015).

[3] D. J. Beebe, J. S. Moore, J. M. Bauer, Q. Yu, R. H. Liu, C. Devadoss, and B.-H. Jo, Nature (London) **404**, 588 (2015).

[4] S. Shan, S. H. Kang, J. R. Raney, P. Wang, L. Fang, F. Candido, J. A. Lewis, and K. Bertoldi, Adv. Mater. **27**, 4296 (2015).

[5] D. Restrepo, N. D. Mankame, and P. D. Zavattieri, Extreme Mech. Lett. **4**, 52 (2015).

[6] B. Florijn, C. Coulais, and M. van Hecke, Phys. Rev. Lett. **113**, 175503 (2014).

[7] K. Bertoldi and M. C. Boyce, Phys. Rev. B **77**, 052105 (2008).

[8] P. Wang, F. Casadei, S. Shan, J. C. Weaver, and K. Bertoldi, Phys. Rev. Lett. **113**, 014301 (2014).

[9] S. Rudykh and M. C. Boyce, Phys. Rev. Lett. **112**, 034301 (2014).

[10] J. Hong, Phys. Rev. Lett. **94**, 108001 (2005).

[11] F. Fraternali, M. Porter, and C. Daraio, Mech. Adv. Mater. Struct. **17**, 1 (2009).

[12] N. Boechler, G. Theocharis, and C. Daraio, Nat. Mater. **10**, 665 (2011).

[13] T. Devaux, V. Tournat, O. Richoux, and V. Pagneux, Phys. Rev. Lett. **115**, 234301 (2015).

[14] F. Li, P. Anzel, J. Yang, P. Kevrekidis, and C. Daraio, Nat. Commun. **5**, 5311 (2014).

[15] A. Spadoni and C. Daraio, Proc. Natl. Acad. Sci. U.S.A. **107**, 7230 (2010).

[16] V. F. Nesterenko, J. Appl. Mech. Tech. Phys. **24**, 733 (1984).

[17] J. Cabaret, V. Tournat, and P. Béquin, Phys. Rev. E **86**, 041305 (2012).

[18] J. Grima and K. Evans, J. Mater. Sci. Lett. **19**, 1563 (2000).

[19] Y. Cho, J.-H. Shin, A. Costa, T. Kim, V. Kunin, J. Li, S. Yeon Lee, S. Yang, H. Han, I.-S. Choi, and D. Srolovitz, Proc. Natl. Acad. Sci. U.S.A. **111**, 17390 (2014).

[20] S. Shan, S. Kang, Z. Zhao, L. Fang, and K. Bertoldi, Extreme Mech. Lett. **4**, 96 (2015).

[21] J. A. Lewis, Adv. Funct. Mater. **16**, 2193 (2006).

[22] J. R. Raney and J. A. Lewis, MRS Bull. **40**, 943 (2015).

[23] See Supplemental Material at http://link.aps.org/supplemental/10.1103/PhysRevLett.118.204102, which includes Refs. [4, 21, 24], for a description of the experiments, details on the model, and supporting movies.

[24] J. R. Raney, N. Nadkarni, C. Daraio, D. M. Kochmann, J. A. Lewis, and K. B. Bertoldi, Proc. Natl. Acad. Sci. U.S.A. **113**, 9722 (2016).

[25] M. Senn, https://www.mathworks.com/matlabcentral/fileexchange/50994-digital-image-correlation-and-tracking.

[26] T. Dauxois and M. Peyrard, *Physics of Solitons* (Cambridge University Press, Cambridge, England, 1967).

[27] Z. Chen, M. Segev, and D. N. Christodoulides, Rep. Prog. Phys. **75**, 086401 (2012).

[28] S. Manakov, Sov. J. Exp. Theor. Phys. **38**, 248 (1974).

[29] F. Allein, V. Tournat, V. Gusev, and G. Theocharis, Appl. Phys. Lett. **108**, 161903 (2016).

[30] A. Merkel, V. Tournat, and V. Gusev, Phys. Rev. Lett. **107**, 225502 (2011).

B. Deng,[1] J. R. Raney,[2] V. Tournat,[1,3] and K. Bertoldi[1,4]

[1]*Harvard John A. Paulson School of Engineering and Applied Science, Harvard University, Cambridge, MA 02138*
[2]*Department of Mechanical Engineering and Applied Mechanics,*
University of Pennsylvania, Philadelphia, PA 19104
[3]*LAUM, CNRS, Université du Maine, Av. O. Messiaen, 72085 Le Mans, France*
[4]*Kavli Institute, Harvard University, Cambridge, MA 02138*
(Dated: 26th April 2017)

FABRICATION

We make use of an extrusion-based 3D printing technique known as direct ink writing to produce the structures in this work. Unlike many conventional commercial 3D printers that rely on either temperature changes or photo-polymerization, direct ink writing is an ambient process that relies on material rheology to produce a pattern that maintains its shape [1]. Subsequent immobilization steps (thermal crosslinking, sintering, etc.) can then be taken after the pattern is formed, in a materials-dependent manner. The advantage of this approach is the broader palette of materials that is compatible with it. Polydimethylsiloxane (PDMS) is a well-behaved silicone rubber that possesses the necessary elastomeric qualities for our structures. However, its conventional precursors are Newtonian fluids that do not maintain their shape after extrusion. A 3D-printable "ink" version of PDMS can be produced through the addition of fumed silica to the resin, resulting in a non-Newtonian paste. Our ink was produced by blending commercially-available PDMS materials (85 wt% Dow Corning SE-1700 and 15 wt% Dow Corning Sylgard 184) in a mixer (Flacktek SpeedMixer). This results in a rheological profile that includes both shear-thinning effects as well as viscoelastic yielding behavior (see SI of Ref. [2] for more details). A shear-thinning response, defined by a decrease in apparent viscosity with increasing shear rate, facilitates extrusion of the material through tapered nozzles (in this case 0.84 mm diameter) during printing. The viscoelastic yielding behavior is characterized by a high storage modulus (G') when shear stress is low (such that the material maintains its shape and behaves like an elastic solid) and a defined yield stress above which the storage modulus suddenly drops (allowing flowability).

The paste-like material therefore flows well during extrusion, but maintains its shape when patterned in 3D. Patterning is performed by a commercial 3D motion control system, which is controlled by G code commands which we generated via python scripts. After the material is patterned, a cross-linking step (100 °C for approximately 30 minutes) produces the familiar hyperelastic mechanical response of PDMS. After curing, additional structural features can be added, for example, through the addition of additional PDMS (Sylgard 184) and (optionally) Cu cylinders that add nodal mass and facilitate motion tracking during subsequent experiments (as in Ref. [3]).

To characterize the response of the two cured PDMS variants (i.e. the standard cast and printed PDMS) used in our structures, we performed dynamic mechanical analysis (DMA) using a TA Instruments RSA III in compression mode. A nominal 100 kPa pre-stress was used, and oscillations of 0.001 strain were imposed up to approximately 90 Hz at room temperature. As shown in Fig. S1, we measured the storage and loss moduli over the relevant frequency range. There is negligible difference between the standard variety of PDMS (indicated as "PDMS (control)") and the silica-filled variety (indicated as "PDMS (printed)") that we use as a 3D printing ink.
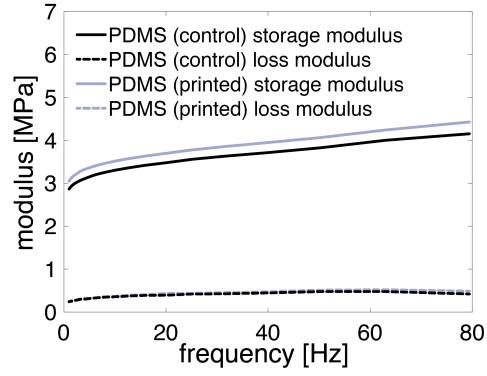
Figure S1: Storage and loss moduli of the cured PDMS materials used in this work. PDMS (control) refers to standard cast PDMS (used in the centers of the squares) while PDMS (printed) refers to the silica-filled PDMS used during 3D printing of the structure.

ADDITIONAL EXPERIMENTAL RESULTS

Input signals

In Fig. S2 we report the input displacement profile, $u_1(t)$, and the corresponding velocity profile, $v_1(t)$, for the five experiments presented in Fig. 2(b). It should be noted that all profiles present similar features. Note that the displacement profile for the impact characterized by $(u_1^{max}, v_1^{max}) = (4.10$ mm, 1166 mm/s) has a very similar shape as $tanh$ function and therefore produces the best solitary wave.
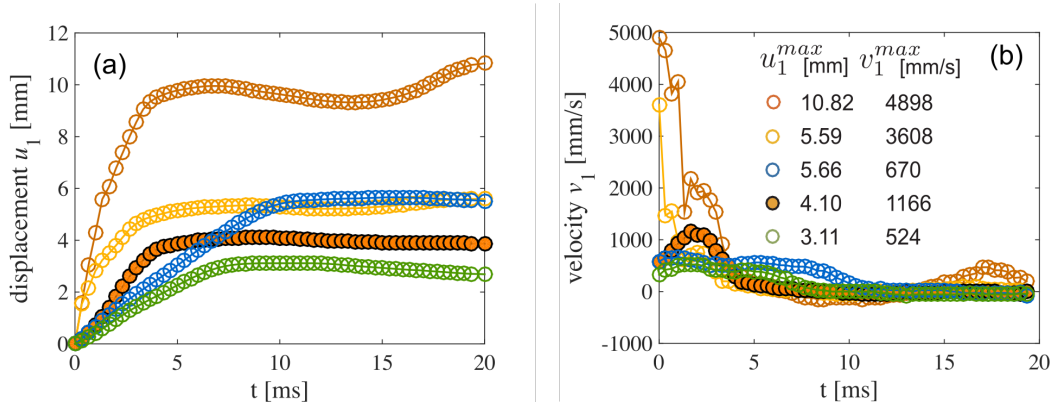
Figure S2: (a) Input displacement profile $u_1(t)$ and (b) corresponding velocity profile $v_1(t)$ for the five experiments presented in Fig. 2(b).

Rotation of the squares

Movies S1 and S2 reveal that the squares not only move horizontally when the pulse propagates, but also rotate. To capture the rotational waves propagating through the sample we conduct an additional set of experiments where the camera is focused only on three squares located at two-thirds of the sample (i.e. the 20th, 21st and 22nd square), as shown in Fig. S3(a) (see also Movie S3). To capture the rotational waves propagating through the sample, we track the positions of two diametrically opposed markers on the copper cylinders, highlighted by red dots and labelled as "top" and "bottom" in Fig. S3(a). The rotation θ_j of the j-th square is then obtained as

$$\theta_j(t) = (-1)^j \tan^{-1} \left(\frac{\left[x_j^{top}(t) - x_j^{top}(0)\right] - \left[x_j^{bot}(t) - x_j^{bot}(0)\right]}{\left[y_j^{top}(t) - y_j^{top}(0)\right] - \left[y_j^{bot}(t) - y_j^{bot}(0)\right]} \right), \tag{S1}$$

where (x_j^{top}, y_j^{top}) and (x_j^{bot}, y_j^{bot}) ($j = 20, 21$ and 22) denote the positions of the two markers. Furthermore, for the same three squares we also monitored their horizontal displacement, by tracking the horizontal position of the marker at the center of the copper cylinders (highlighted by a red dot and labelled as "center" in Fig. S3(a))

In Figs. S3(b) and (c) we show the evolution of u_j and θ_j as a function of time, respectively. The results confirm the simultaneous propagation of translational and rotational waves in our structure.
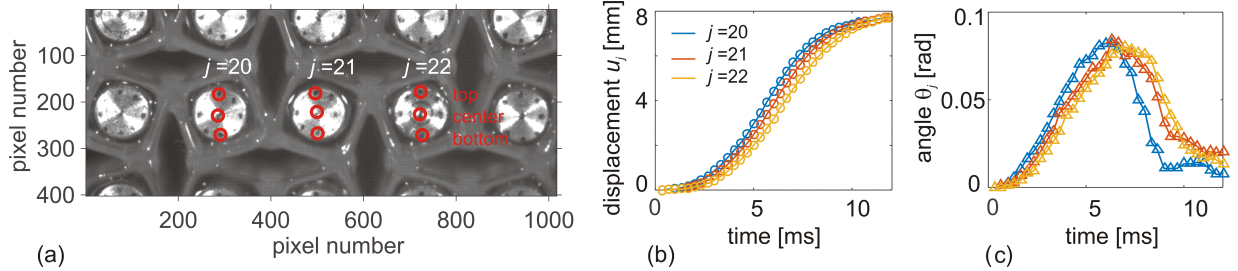
Figure S3: (a) Movie frame: three squares are analyzed (i.e. the 20th, 21st and 22nd squares). For each unit cell three markers (red dots) are tracked. (b) Extracted horizontal displacements u_j and (c) angles θ_j as a function of time.

ANALYTICAL EXPLORATION

To get a deeper understanding of the mechanical response of the structure, we analytically investigate its behavior. We first establish a discrete model and determine the governing equations. Then, we take the continuum limit and derive analytical solutions.

Discrete model

Our structure consists of a network of square domains connected by thin ligaments (see Fig. 1 of the main text and Figure S4-a), all made of elastomeric material (polydimethylsiloxane - PDMS). The squares have diagonal lengths of $2l$ that are rotated by an angle θ_0 with respect to the horizontal direction. In this study we are investigating the propagation of plane waves along the x-direction. To efficiently model the system, we first notice that when a planar wave propagates through the system all deformation is localized at the hinges that bend in-plane, inducing pronounced rotations of the squares. Therefore, the structure can be modeled as a network of rigid squares connected by springs at their vertices (see Figure S4-b). More specifically, we model each hinge with two linear springs: (i) a compression/tension spring with stiffness k and (ii) a torsional one with stiffness k_θ.

Finally, we also find that, when a planar wave propagates in the x-direction, (i) the squares do not move in the y-direction; (ii) neighboring squares aligned vertically experience the same horizontal displacement and rotate by the same amount but in opposite directions; and (iii) neighboring squares always rotate in opposite directions. Therefore, since in this study we focus on the propagation of planar waves in the x-direction, each rigid square in our discrete model has two degrees of freedom: the displacement in the x-direction, u, and the rotation about the z-axis, θ. Moreover, focusing on the rigid $[j, i]$-th square (see Figure S4), we have

$$u^{[j, i]} = u^{[j, i+1]}, \quad \theta^{[j, i]} = \theta^{[j, i+1]}. \tag{S2}$$

Note that, as indicated by the blue and red arrows in Fig. S4, we define positive direction of rotation alternatively for neighboring squares (i.e., if for the $[j, i]$-th square a clockwise rotation is positive, then for $[j, i-1]$-th, $[j, i+1]$-th, $[j+1, i]$-th and $[j-1, i]$-th ones counterclockwise rotation is considered as positive). We found this choice to facilitate our analysis.
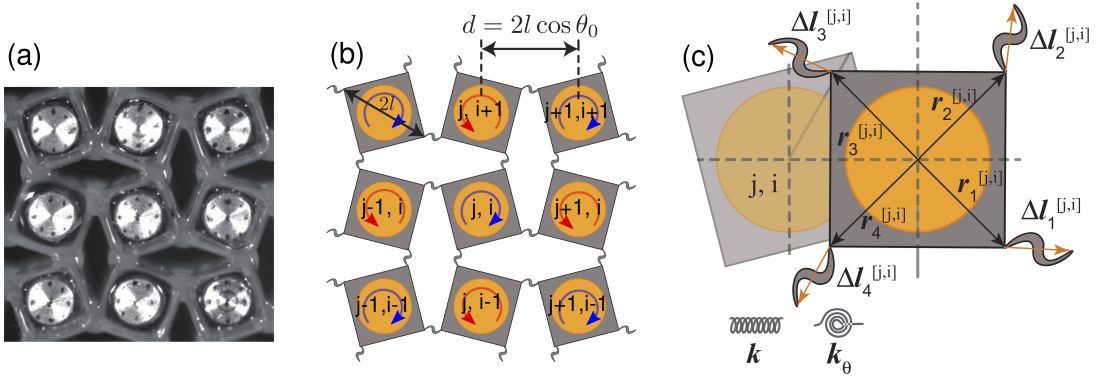
Figure S4: (a) Picture of our structure. (b)-(c) Schematics of the system.

Governing equations of the discrete model

To determine the governing equations for the discrete model, we focus on the $[j, i]$-th rigid square, for whose behavior is governed by

$$m^{[j, i]}\ddot{u}^{[j, i]} = \sum_{p=1}^{4} F_p^{[j, i]},$$

$$J^{[j, i]}\ddot{\theta}^{[j, i]} = \sum_{p=1}^{4} M_p^{[j, i]},$$

(S3)

where $m^{[j, i]}$ and $J^{[j, i]}$ are the mass and moment of inertia of the rigid square, respectively. Moreover, $F_p^{[j, i]}$ and $M_p^{[j, i]}$ are the forces in horizonal direction and moments generated at the p-th vertex of the rigid square by the tension/compression and torsional springs, respectively. To calculate these forces and moments, we start by determining the vectors $\mathbf{r}_p^{[j, i]}$ (p=1, 2, 3, 4) that connect the center of the $[i, j]$-th rigid square to its four vertices (see Fig. S4-c),

$$\mathbf{r}_1^{[j, i]}(\theta^{[j, i]}) = l\left[\cos(\theta^{[j, i]} + \theta_0)\right]\mathbf{e}_x + l\left[(-1)^j\sin(\theta^{[j, i]} + \theta_0)\right]\mathbf{e}_y,$$

$$\mathbf{r}_2^{[j, i]}(\theta^{[j, i]}) = l\left[-(-1)^j\sin(\theta^{[j, i]} + \theta_0)\right]\mathbf{e}_x + l\left[\cos(\theta^{[j, i]} + \theta_0)\right]\mathbf{e}_y,$$

$$\mathbf{r}_3^{[j, i]}(\theta^{[j, i]}) = l\left[-\cos(\theta^{[j, i]} + \theta_0)\right]\mathbf{e}_x + l\left[-(-1)^j\sin(\theta^{[j, i]} + \theta_0)\right]\mathbf{e}_y,$$

$$\mathbf{r}_4^{[j, i]}(\theta^{[j, i]}) = l\left[(-1)^j\sin(\theta^{[j, i]} + \theta_0)\right]\mathbf{e}_x + l\left[-\cos(\theta^{[j, i]} + \theta_0)\right]\mathbf{e}_y,$$

(S4)

The deformation of the springs connected to the vertices of the rigid square can then be written as

$$\boldsymbol{\Delta}\mathbf{l}_1^{[j, i]} = \left(u^{[j+1, i]} - u^{[j, i]}\right)\mathbf{e}_x + \left[\left(\mathbf{r}_3^{[j+1, i]}(\theta^{[j+1, i]}) - \mathbf{r}_3^{[j+1, i]}(0)\right) - \left(\mathbf{r}_1^{[j, i]}(\theta^{[j, i]}) - \mathbf{r}_1^{[j, i]}(0)\right)\right]$$

$$\Delta\theta_1^{[j, i]} = \theta^{[j, i]} + \theta^{[j+1, i]}$$

$$\boldsymbol{\Delta}\mathbf{l}_2^{[j, i]} = \left[\left(\mathbf{r}_4^{[j, i+1]}(\theta^{[j, i+1]}) - \mathbf{r}_4^{[j, i+1]}(0)\right) - \left(\mathbf{r}_2^{[j, i]}(\theta^{[j, i]}) - \mathbf{r}_2^{[j, i]}(0)\right)\right]$$

$$\Delta\theta_2^{[j, i]} = \theta^{[j, i]} + \theta^{[j, i+1]}$$

$$\boldsymbol{\Delta}\mathbf{l}_3^{[j, i]} = \left(u^{[j-1, i]} - u^{[j, i]}\right)\mathbf{e}_x + \left[\left(\mathbf{r}_1^{[j-1, i]}(\theta^{[j-1, i]}) - \mathbf{r}_1^{[j-1, i]}(0)\right) - \left(\mathbf{r}_3^{[j, i]}(\theta^{[j, i]}) - \mathbf{r}_3^{[j, i]}(0)\right)\right]$$

$$\Delta\theta_3^{[j, i]} = \theta^{[j, i]} + \theta^{[j-1, i]}$$

$$\boldsymbol{\Delta}\mathbf{l}_4^{[j, i]} = \left[\left(\mathbf{r}_2^{[j, i-1]}(\theta^{[j, i-1]}) - \mathbf{r}_2^{[j, i-1]}(0)\right) - \left(\mathbf{r}_4^{[j, i]}(\theta^{[j, i]}) - \mathbf{r}_4^{[j, i]}(0)\right)\right]$$

$$\Delta\theta_4^{[j, i]} = \theta^{[j, i]} + \theta^{[j, i-1]}$$

(S5)

where $\boldsymbol{\Delta l}_p^{[m,\,n]}$ and $\Delta\theta_p^{[m,\,n]}$ denote the changes in length and angle experienced by the tension/compression and rotational springs on the p-th vertex of $[m,\,n]$-th rigid square, respectively. It follows that

$$F_p^{[j,\,i]} = \left(k\boldsymbol{\Delta l}_p^{[j,\,i]} + \frac{k_\theta\Delta\theta_p^{[j,\,i]}}{l^2}\left(\mathbf{e}_z\times\mathbf{r}_p^{[j,\,i]}\right)\right)\cdot\mathbf{e}_x,$$

$$M_p^{[j,\,i]} = -k_\theta\Delta\theta_p^{[j,\,i]} - k\,\mathbf{r}_p^{[j,\,i]}\times\boldsymbol{\Delta l}_p^{[j,\,i]}.$$

(S6)

Substitution of Eqns. (S6) and (S2) into Eqns. (S3) yields

$$
\begin{aligned}
m^{[j,\,i]}\ddot{u}^{[j,\,i]} &= k\left(u^{[j+1,\,i]} - 2u^{[j,\,i]} + u^{[j-1,\,i]} - l\cos(\theta^{[j+1,\,i]}+\theta_0) + l\cos(\theta^{[j-1,\,i]}+\theta_0)\right)\\
&\quad + \frac{k_\theta}{l}\left(\theta^{[j-1,\,i]} - \theta^{[j+1,\,i]}\right)\sin(\theta^{[j,\,i]}+\theta_0),\\
J^{[j,\,i]}\ddot{\theta}^{[j,\,i]} &= -k_\theta\left(\theta^{[j+1,\,i]} + 6\theta^{[j,\,i]} + \theta^{[j-1,\,i]}\right) - kl\left(u^{[j+1,\,i]} - u^{[j-1,\,i]}\right)\sin(\theta^{[j,\,i]}+\theta_0)\\
&\quad + kl^2\sin(\theta^{[j,\,i]}+\theta_0)\left(\cos(\theta^{[j+1,\,i]}+\theta_0) + 6\cos(\theta^{[j,\,i]}+\theta_0) + \cos(\theta^{[j-1,\,i]}+\theta_0) - 8\cos(\theta_0)\right).\\
&\quad + kl^2\cos(\theta^{[j,\,i]}+\theta_0)\left(\sin(\theta^{[j+1,\,i]}+\theta_0) + \sin(\theta^{[j-1,\,i]}+\theta_0) - 2\sin(\theta^{[j,\,i]}+\theta_0)\right)
\end{aligned}
$$

(S7)

which represent the governing equations for the discrete system.

Continuum limit

While Eqs. (S7) contains the full nonlinear and dispersive terms of the modeled system and can only be solved numerically, a deeper insight into the system dynamics can be achieved by further simplifying them to derive analytical solutions. To this end, we fist introduce the normalized displacement $U^{[j,\,i]} = u^{[j,\,i]}/(2l\cos\theta_0)$, time $T = t\sqrt{k/m}$, stiffness $K = k_\theta/(kl^2)$ and inertia $\alpha = l\sqrt{m/J}$. Moreover, since in Eqs. (S7) only the displacements and rotations of squares in the i-th appear, for the sake of simplicity we set $U_j = U^{[j,\,i]}$, and $\theta_j = \theta^{[j,\,i]}$. The governing equations Eqs. (S7) can be then be written in dimensionless form as

$$
\begin{aligned}
\frac{\partial^2 U_j}{\partial T^2} &= U_{j+1} - 2U_j + U_{j-1} - \frac{1}{2\cos(\theta_0)}\left[\cos(\theta_{j+1}+\theta_0) - \cos(\theta_{j-1}+\theta_0) + K\left(\theta_{j+1} - \theta_{j-1}\right)\sin(\theta_j+\theta_0)\right]\\
\frac{\partial^2\theta_j}{\partial T^2} &= \alpha^2\Bigg\{-K(\theta_{j+1} + 6\theta_j + \theta_{j-1}) - 2(U_{j+1} - U_{j-1})\cos(\theta_0)\sin(\theta_j+\theta_0)\\
&\quad + \sin(\theta_j+\theta_0)\Big[\cos(\theta_{j+1}+\theta_0) + 6\cos(\theta_j+\theta_0) + \cos(\theta_{j-1}+\theta_0) - 8\cos(\theta_0)\Big]\\
&\quad + \cos(\theta_j+\theta_0)\Big[\sin(\theta_{j+1}+\theta_0) + \sin(\theta_{j-1}+\theta_0) - 2\sin(\theta_j+\theta_0)\Big]\Bigg\}.
\end{aligned}
$$

(S8)

Next , we introduce two continuous functions $U(X)$ and $\theta(X)$, which interpolate the discrete variables U_j and θ_j as

$$U(X_j) = U_j, \quad \text{and} \quad \theta(X_j) = \theta_j,$$

(S9)

where $X_j = x_j/2l\cos(\theta_0)$ denotes the normalized coordinate along the x-axis. Using Taylor expansion, the displacement U and rotation θ in correspondence of the $(j-1)$-th and $(j+1)$-th squares can then be expressed as

$$
\begin{aligned}
U(X_{j-1}) &\approx U(X_j) - \left.\frac{\partial U}{\partial X}\right|_{X=X_j} + \frac{1}{2}\left.\frac{\partial^2 U}{\partial X^2}\right|_{X=X_j},\\
U(X_{j+1}) &\approx U(X_j) + \left.\frac{\partial U}{\partial X}\right|_{X=X_j} + \frac{1}{2}\left.\frac{\partial^2 U}{\partial X^2}\right|_{X=X_j},\\
\theta(X_{j-1}) &\approx \theta(X_j) - \left.\frac{\partial\theta}{\partial X}\right|_{X=X_j} + \frac{1}{2}\left.\frac{\partial^2\theta}{\partial X^2}\right|_{X=X_j},\\
\theta(X_{j+1}) &\approx \theta(X_j) + \left.\frac{\partial\theta}{\partial X}\right|_{X=X_j} + \frac{1}{2}\left.\frac{\partial^2\theta}{\partial X^2}\right|_{X=X_j},
\end{aligned}
$$

(S10)

from which the derivatives of U and θ are obtained as

$$
\begin{aligned}
\left.\frac{\partial U}{\partial X}\right|_{X=X_j} &\approx \frac{1}{2}\left[U\left(X_{j+1}\right)-U\left(X_{j-1}\right)\right], \\
\left.\frac{\partial^2 U}{\partial X^2}\right|_{X=X_j} &\approx U\left(X_{j+1}\right)-2U\left(X_j\right)+U\left(X_{j-1}\right), \\
\left.\frac{\partial \theta}{\partial X}\right|_{X=X_j} &\approx \frac{1}{2}\left[\theta\left(X_{j+1}\right)-\theta\left(X_{j-1}\right)\right], \\
\left.\frac{\partial^2 \theta}{\partial X^2}\right|_{X=X_j} &\approx \theta\left(X_{j+1}\right)-2\theta\left(X_j\right)+\theta\left(X_{j-1}\right).
\end{aligned}
\tag{S11}
$$

Moreover, to further simplify the equations, we assume that the rotation angle θ is small, so that $\sin\theta \sim \theta$ and $\cos\theta \sim 1$. It follows that

$$
\begin{aligned}
\sin(\theta_j + \theta_0) &\approx \sin\theta_0 + \theta_j \cos\theta_0, \\
\cos(\theta_j + \theta_0) &\approx \cos\theta_0 - \theta_j \sin\theta_0.
\end{aligned}
\tag{S12}
$$

Finally, we substitute Eqs. (S11) and (S12) into the discrete governing equations (Eqs.(S8)) and retain the nonlinear terms up to the second order as well as the dominant dispersion terms, obtaining

$$
\begin{aligned}
\frac{\partial^2 U}{\partial T^2} &= \frac{\partial^2 U}{\partial X^2} + (1-K)\tan(\theta_0)\frac{\partial \theta}{\partial X}, \\
\frac{\partial^2 \theta}{\partial T^2} &= \alpha^2\left[(\cos(2\theta_0)-K)\frac{\partial^2 \theta}{\partial X^2} - 2\sin(2\theta_0)\frac{\partial U}{\partial X} - 4\left(2K + \cos^2(\theta_0)\frac{\partial U}{\partial X} + 2\sin^2(\theta_0)\right)\theta - 4\sin(2\theta_0)\theta^2\right],
\end{aligned}
\tag{S13}
$$

which represent the continuum governing equations of the system.

Next, we introduce the travelling wave coordinate $\zeta = X - cT$, c being the normalized pulse velocity (the real pulse velocity is $c\,2l\sqrt{k/m}$), so that Eqs. (S13) become

$$
\frac{\partial^2 U}{\partial \zeta^2} = -\frac{(1-K)\tan(\theta_0)}{1-c^2}\frac{\partial \theta}{\partial \zeta},
\tag{S14}
$$

$$
\frac{\partial^2 \theta}{\partial \zeta^2} = 2\alpha^2\beta\sin(2\theta_0)\frac{\partial U}{\partial \zeta} + 4\alpha^2\beta\sin(2\theta_0)\theta^2 + 4\alpha^2\beta[2K + \cos^2(\theta_0)\frac{\partial U}{\partial \zeta} + 2\sin^2(\theta_0)]\theta,
\tag{S15}
$$

where

$$
\beta = \frac{1}{\alpha^2(\cos(2\theta_0)-K)-c^2}.
\tag{S16}
$$

Note that the displacement U and rotation θ are now continuous functions of ζ and T. Integration of Eq. (S14) with respect to ζ, with the assumption of a zero integration constant (i.e. a wave with a finite temporal and spatial support), yields

$$
\frac{\partial U}{\partial \zeta} = -\frac{(1-K)\tan\theta_0}{1-c^2}\theta,
\tag{S17}
$$

which can then be substituted into Eq. (S15) to obtain

$$
\frac{\partial^2 \theta}{\partial \zeta^2} + P\theta + Q\theta^2 = 0,
\tag{S18}
$$

where

$$
\begin{aligned}
P &= \frac{4\alpha^2\beta}{(1-c^2)}\left[(2c^2-1-K)\sin^2\theta_0 - 2(1-c^2)K\right], \\
Q &= \frac{2\alpha^2\beta}{(1-c^2)}(2c^2-1-K)\sin(2\theta_0).
\end{aligned}
\tag{S19}
$$

Note that for $\theta_0 \to 0$, $Q \to 0$ and Eq. (S18) becomes a linear equation. Therefore, the analytical solution derived here is not valid when $\theta_0 \to 0$, since the cubic term, which is omitted here, must be considered to properly describe the propagation of nonlinear waves in such structures.

Eq. (S18) has the form of the well-known nonlinear Klein-Gordon equation with quadratic nonlinearity. When $P < 0$ and $Q > 0$, analytical solutions of Eq. (S18) exist in the form of a finite amplitude solitary wave with a stable profile

$$\theta = A \operatorname{sech}^2 \frac{\zeta}{W}, \tag{S20}$$

where A, c and W denotes the amplitude, velocity and characteristic width of the wave (note that solutions for $P < 0$ and $Q < 0$ also exist, but are diverging for $\zeta \to 0$). Moreover, by substituting Eq.(S20) into Eq. (S17) the solution for the displacement is found as

$$U = A \frac{(1 - K)W \tan(\theta_0)}{(1 - c^2)} \left[1 - \tanh\left(\frac{\zeta}{W} \right) \right]. \tag{S21}$$

Note that the pulse velocity c and width W depend both on the amplitude A of the wave and the geometry of the structure (i.e. α, K and θ_0). In fact, substitution of Eq. (S20) into Eq. (S18) yields

$$A \left(P + \frac{4}{W^2} \right) \operatorname{sech}^2 \frac{\zeta}{W} + A \left(AQ - \frac{6}{W^2} \right) \operatorname{sech}^4 \frac{\zeta}{W} = 0, \tag{S22}$$

which is satisfied for any ζ only if

$$P + \frac{4}{W^2} = 0, \quad \text{and} \quad AQ - \frac{6}{W^2} = 0. \tag{S23}$$

By substituting Eqs. (S19) into Eqs. (S23), we finally find

$$
\begin{aligned}
c &= \sqrt{\frac{6K + 3(1 + K)\sin^2(\theta_0) + A(1 + K)\sin(2\theta_0)}{6K + 6\sin^2(\theta_0) + 2A\sin(2\theta_0)}}, \\
W &= \frac{1}{\alpha} \sqrt{\frac{(1 - c^2)[\alpha^2(\cos(2\theta_0) - K) - c^2]}{2(1 - c^2)K + (1 - 2c^2 + K)\sin^2(\theta_0)}}
\end{aligned}
\tag{S24}
$$

In Fig. S5 we report the evolution of c and W as predicted by Eqs. (S24). In Figs. S5-a and -d we consider $K = 0.073$, $\alpha = 1.70$ and report the evolution of W and c as a function of A and θ_0. Note that we consider $5° < \theta_0 < 30°$. The lower limit for θ_0 is dictated by the fact that Eq. (S18) is not valid when $\theta_0 \to 0$ (since the quadratic term vanished in this case), while the upper limit is determined by noting that, for this particular choice of K and α, the characteristic width W is an imaginary number for $\theta_0 > 36.7°$ (indicating that the solitons no longer exist for $\theta_0 > 36.7°$). In Fig. S5-b and -e we consider $\theta_0 = 25°$ and $\alpha = 1.70$ and report the evolution of W and c as a function of A and K. Finally, in Fig. S5-c and -f we consider $\theta_0 = 25°$, $K = 0.073$ and report the evolution of W and c as a function of A and α. Note that the structure used in this study is characterized by $\theta_0 = 25°$, $\alpha = 1.70$ and $K = 0.073$.

The contour plots reveal that the pulse speed c is not significantly affected by the amplitude A. In contrast, A has an important effect on W, that is found to dramatically increase as the pulse amplitude decreases. In fact, the results of Figs. S5-a, -b and -c indicate that $W \to \infty$ as $A \to 0$. Note that as $A \to 0$ the nonlinear response of the system is weakly activated and W needs to be very large (a low frequency or long wavelength pulse) to ensure a balancing weak dispersion. As such, solitary waves are expected to form only after long propagation distances, even for excitations very close to the ideal ones. Experimentally, this requires very long samples, but then the pulse would be subjected to strong damping, posing serious limitations to the observation and existence of small amplitude solitary waves. Moreover, we find that the pulse width W can also be tuned by changing the stiffness parameter K. Our results indicate that c is affected by changes in both θ_0 and K.

It is important to note that the existence of the solitary solution to the Klein-Gordon equation (Eq. (S18)) requires that

$$
\begin{aligned}
P &= \frac{4\alpha^2 \beta}{(1 - c^2)} \left[(2c^2 - 1 - K)\sin^2\theta_0 - 2(1 - c^2)K \right] < 0, \\
Q &= \frac{2\alpha^2 \beta}{(1 - c^2)}(2c^2 - 1 - K)\sin(2\theta_0) > 0.
\end{aligned}
\tag{S25}
$$

By substituting Equation (S24)$_1$ into Equation (S25), we obtain two non-linear inequalities in A, α, K and θ_0. The structure supports a soliton if these two inequalities are satisfied for all amplitudes $A < \pi/4 - \theta_0$, where the constraint is introduced to avoid contact between neighboring squares. We find that the system supports a soliton for $\alpha \in [1.09, \infty)$, $K \in [0, 0.336]$ and $\theta_0 \in [0°, 36.7°]$. Note that the system considerd in this study is characterized by $\alpha = 1.70$, $K = 0.073$ and $\theta_0 = 25°$.
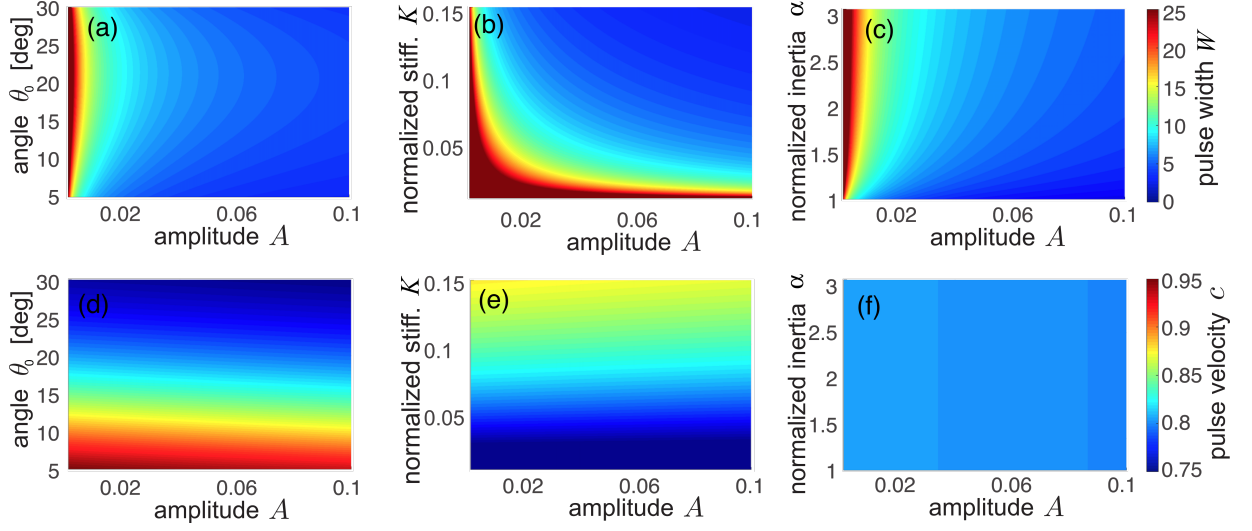
Figure S5: Contour plots showing the evolution of c and W. (a) Evolution of W as a function of A and θ_0 (assuming $K = 0.073$ and $\alpha = 1.70$). (b) Evolution of W as a function of A and K (assuming $\theta_0 = 25°$ and $\alpha = 1.70$). (c) Evolution of W as a function of A and α (assuming $\theta_0 = 25°$ and $K = 0.073$). (d) Evolution of c as a function of A and θ_0 (assuming $K = 0.073$ and $\alpha = 1.70$). (e) Evolution of c as a function of A and K (assuming $\theta_0 = 25°$ and $\alpha = 1.70$). (f) Evolution of c as a function of A and α (assuming $\theta_0 = 25°$ and $K = 0.073$).
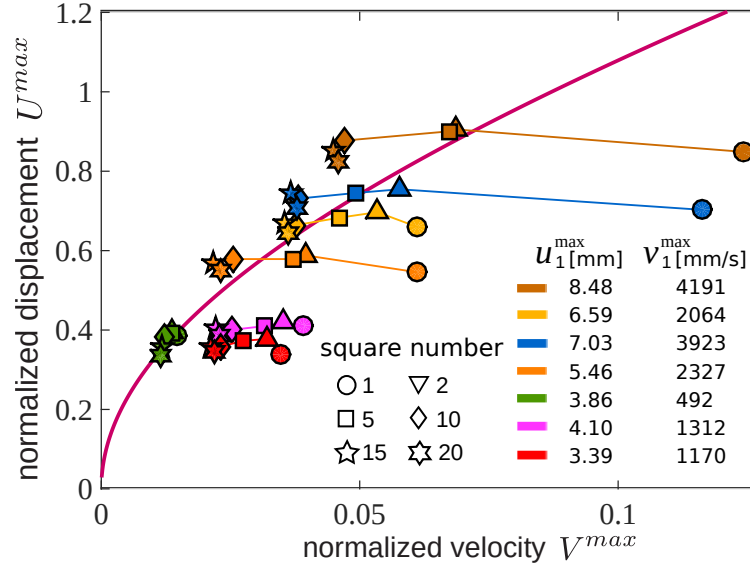
Figure S6: Comparison between analytical solution (continuous line) and experimental results (markers). Experimental results are reported for seven different impacts characterized by different combinations of u_1^{max} and v_1^{max}.

Finally, we note that the maximum displacement and velocity induced by the pulse, U^{max} and V^{max}, can be

obtained from Eq. (S21) as

$$U^{max} = \max(U) = 2A\frac{(1-K)W\tan(\theta_0)}{(1-c^2)}$$
$$V^{max} = \max\left(\frac{dU}{dT}\right) = cA\frac{(1-K)\tan(\theta_0)}{(1-c^2)} \tag{S26}$$

so that

$$\frac{U^{max}}{V^{max}} = \frac{2W}{c} = \frac{2}{\alpha}\sqrt{\frac{\left[6K + 6\sin^2(\theta_0) + 2A\sin(2\theta_0)\right]\left[(1-c^2)[\alpha^2\left(\cos(2\theta_0) - K\right) - c^2]\right]}{\left[6K + 3\left(1+K\right)\sin^2(\theta_0) + A\left(1+K\right)\sin(2\theta_0)\right]\left[2(1-c^2)K + (1-2c^2+K)\sin^2(\theta_0)\right]}}. \tag{S27}$$

Eqn. (S27) defines a parametric representation of a curve, where A is the parameter. Such a curve is plotted in Fig. 4 of the main text with results from five different experiments and in Fig. S6 together with results from another seven experiments. Note that the experimental data (markers) are obtained by monitoring the maximum displacement and velocity experienced by the 1st, 2nd, 5th, 10th, 15th and 20th squares. Interestingly, we find that all applied excitations result in the propagation of a soliton. However, it is important to note that this observation is not general and related to the limited variety of excited displacement profiles (all of them are reasonable closed to tanh - see Fig. S2). When in our numerical simulations we use an input displacement profile very different from tanh,

$$U_1(T) = \text{sech}\frac{T}{B}, \tag{S28}$$

B being a constant, solitons are not generated (see Fig. S7).
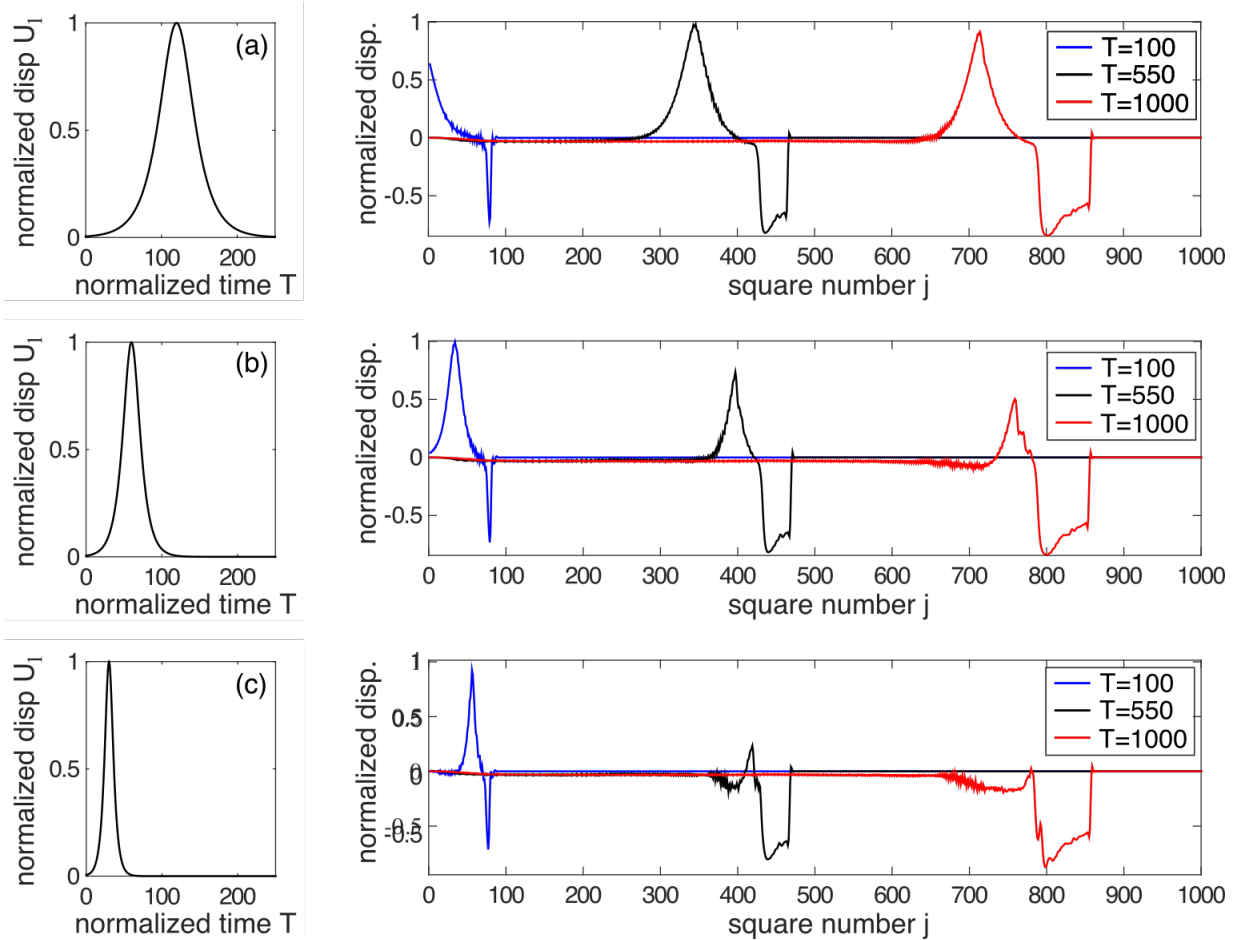
Figure S7: Response of the system for excited displacement profile with the form of the sech function. The profile displacement is defined as $U_1(T) = \text{sech}(T/B)$ with (a) $B = 20$, (b) $B = 10$ and (c) $B = 5$.

Propagation of small amplitude waves

As discussed above, for sufficiently small amplitudes the propagating elastic waves do not excite the nonlinear response of the system. As such, in this case we expect small amplitude dispersive waves and not stable solitary waves to propagate through the structure.

To better understand how elastic waves with sufficiently small amplitudes propagate through the system, we make use of Eqs. (S12) and linearize the discrete governing equations (S8) to obtain

$$\frac{\partial^2 U_j}{\partial T^2} = U_{j+1} - 2U_j + U_{j-1} + \frac{1}{2}\tan(\theta_0)\left(1 - K\right)\left(\theta_{j+1} - \theta_{j-1}\right),$$
$$\frac{\partial^2 \theta_j}{\partial T^2} = \alpha^2 \left[\left(\cos^2(2\theta_0) - K\right)\left(\theta_{j+1} + \theta_{j-1}\right) - 2\left(1 + 2\sin^2(\theta_0) + 3K\right)\theta_j - \sin(2\theta_0)\left(U_{j+1} - U_{j-1}\right)\right].$$

(S29)

Eqs. (S29) can be written in matrix form as

$$\mathbf{M}\ddot{\mathbf{U}}_j + \sum_{p=-1,0,1} \mathbf{K}^{(p)}\mathbf{U}_{j+p} = 0$$

(S30)

where

$$\mathbf{M} = \begin{bmatrix} 1 & 0 \\ 0 & 1 \end{bmatrix}, \quad \ddot{\mathbf{U}}_{j+p} = \begin{bmatrix} \frac{\partial^2 U_{j+p}}{\partial T^2} \\ \frac{\partial^2 \theta_{j+p}}{\partial T^2} \end{bmatrix}, \quad \mathbf{U}_{j+p} = \begin{bmatrix} U_{j+p} \\ \theta_{j+p,} \end{bmatrix}, \quad \mathbf{K}^{-1} = \begin{bmatrix} -1 & \frac{1}{2}\left(1 - K\right)\tan(\theta_0) \\ -\alpha^2\sin(2\theta_0) & -\alpha^2(\cos(2\theta_0) - K) \end{bmatrix}$$
$$\mathbf{K}^0 = \begin{bmatrix} 2 & 0 \\ 0 & 2\alpha^2(1 + 2\sin^2(\theta_0) + 3K) \end{bmatrix}, \quad \mathbf{K}^1 = \begin{bmatrix} -1 & -\frac{1}{2}\left(1 - K\right)\tan(\theta_0) \\ \alpha^2\sin(2\theta_0) & -\alpha^2(\cos(2\theta_0) - K) \end{bmatrix}$$

(S31)

Next, we seek a solution in the form of a harmonic wave

$$\mathbf{U}_{j+p}(T) = \tilde{\mathbf{U}}(\mu)\exp i(\mu X_{j+p} - \omega T)$$

(S32)

where ω is the temporal frequency of harmonic motion, μ is the wavenumber and $\tilde{\mathbf{U}}$ is a complex quantity that defines the amplitude of wave motion. Substitution of Eq. (S32) into Eq. (S30) yields

$$-\omega^2\mathbf{M}\ddot{\mathbf{U}}_j + \sum_{p=-1,0,1} \mathbf{K}^{(p)}e^{p\mu} = 0$$

(S33)

which can be solved numerically for wavenumbers $\mu \in [0, \pi]$ to obtain the dispersion relation curves shown in Fig. S8-a. Note that in this band structure the frequency ω is normalised by $\sqrt{k/m}$. It is important to point out that the two degrees of freedom of the system are coupled, so that both dispersion curves have translational and rotational components.

Finally, in Fig. S8-b we report the evolution of the group velocity ($c_g = d\omega/dk$) and phase velocity ($c_p = \omega/k$) for the lower branch as a function of the wavenumber. Both velocities are normalized by $2l\sqrt{k/m}$.

Estimation of k and k_θ

To connect the discrete model to our sample, we need to estimate the mass of the squares (m), their rotational inertia (J) and the spring stiffnesses (k and k_θ). The mass m can be easily measured as 2.093 g and the rotational inertia J can be calculated from the geometry of the squares to obtain $J = 18.11$ g·mm^2, so that nondimensional parameter α is determined as $\alpha = l\sqrt{m/J} = 1.70$ (note that l denotes the half length of the square diagonals, $l = 5.517$ mm). To estimate the spring stiffness k, we start by extracting from our experiments the group velocity of the fastest travelling wave packets, $\tilde{c}_g^{max}$. We find that any applied excitation results in $\tilde{c}_g^{max} \approx 29$ m/s. Since the numerical results shown in Fig. S8-b indicate that the maximum normalized group velocity is $c_g^{max} = 0.8670$, it follows that

$$c_g^{max}2l\sqrt{\frac{k}{m}} = 0.8670 \cdot 2 \cdot 0.005517\sqrt{\frac{k}{0.002093}} \approx 29\,\text{m/s}$$

(S34)
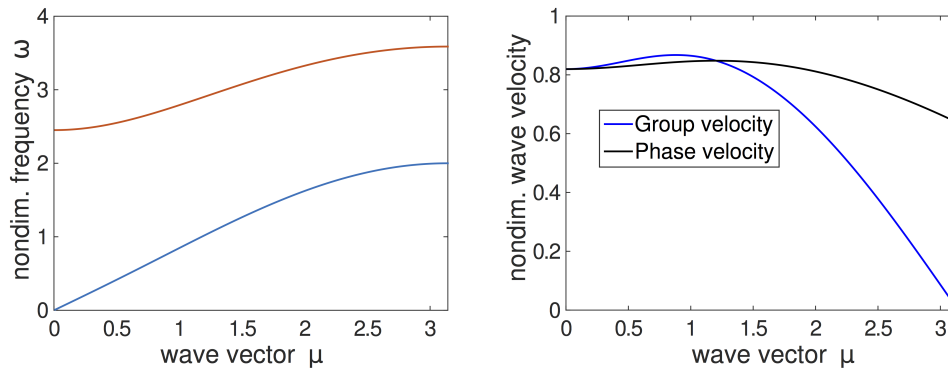
Figure S8: (a) Dispersion curves and (b) evolution of the group and phase velocity for the lower branch as a function of the wavenumber. To generate the plots, we considered K=0.073, α=1.70 and θ_0=25°.

from which we obtain $k = 19235$ N/m.

Having determined k, we then use equilibrium considerations and Finite Element (FE) simulations to obtain k_θ. On the analytical side, since the structure is periodic, we focus on a single square and consider quasi static uniaxial compression along the vertical direction (see Fig. S3-a). For this loading case, a force F is applied to the top and bottom hinges, while there are no forces on the left and right hinges (since the structure is stress-free in horizonal direction). The moment generated by F is therefore balanced by those generated by the four rotational springs, so that

$$\sum M_A = -8k_\theta\theta + 2Fl\sin(\theta_0 + \theta) = 0, \tag{S35}$$

where the reference point A is indicated in Fig. S3-a. It follows from Eq. (S35) that

$$F = \frac{4k_\theta\theta}{l\sin(\theta_0 + \theta)}. \tag{S36}$$

Moreover, the resulting compressive strain ϵ can be written as

$$\begin{aligned}
\epsilon &= \frac{F}{2lk} + (\cos(\theta_0) - \cos(\theta_0 + \theta)) \\
&= \frac{2K\theta}{\sin(\theta_0 + \theta)} + (\cos(\theta_0) - \cos(\theta_0 + \theta))
\end{aligned} \tag{S37}$$

where the first term accounts for the compression of the linear springs and the second one for the rotation of the square. Finally, Eqs.(S36) and (S37) can used to generate the force-strain (F-ϵ) curve, shown as a continuous line in Fig. S9-b.

On the numerical side, we simulate the response of the structure under uniaxial compression using ABAQUS/Standard. To reduce the computational costs and make sure the response of the system is not dominated by boundary effects, we consider a unit cell comprising a 2×2 array of squares with identical geometry as those considered in the experiments and apply periodic boundary conditions. The unit cell is discretized with plane strain triangular elements (ABAQUS element type: CPE6) and the material is modeled using an almost incompressible Neo-Hookean material with initial shear modulus $\mu_0 = 0.32MPa$ [2] . The compressive force as a function of the applied strain is then extracted from the simulation and compared to the analytical prediction. The best agreement between the two curves is found for $k_\theta = 0.0427$ Nm/rad (see Fig. S3-b), so that we obtain $K = k_\theta/kl^2 = 0.073$.
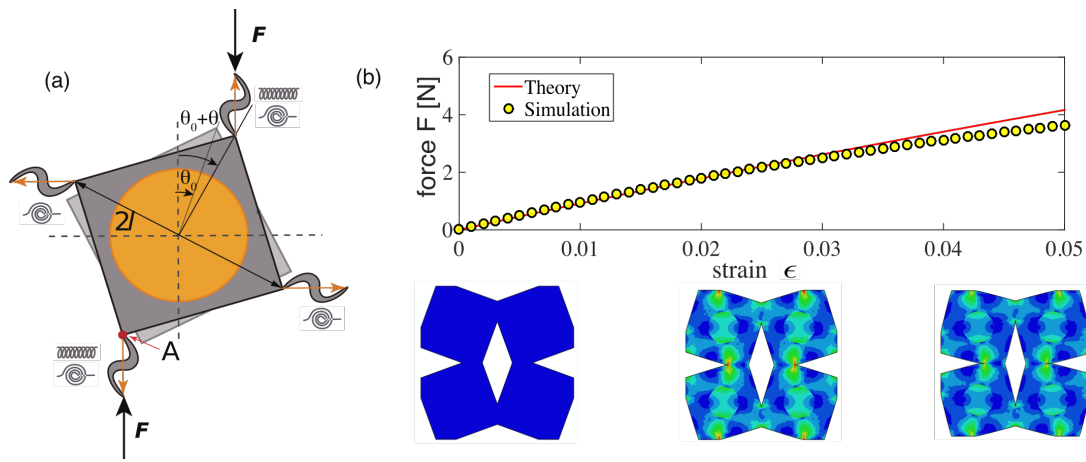
Figure S9: (a) Schematic of an individual square. (b) Force-strain curve under uniaxial compression. Comparison between analytical (continuous line) and numerical (markers) results.

MOVIE CAPTIONS

Movie S1 Experiment in which the impactor prescribes a displacement signal to the first square characterized by (u_1^{max}, v_1^{max})=(3.11 mm, 524 mm/s). Note that after the pulse is applied the squares near the impactor vibrate at high frequency. This is because the applied impact results in a displacement signal that does not exactly match that of the supported solitary wave. Therefore, not all the energy applied by the impactor goes into the soliton and some activates vibrations of the squares near the impactor. It is important to note that these vibrations have frequencies in the range of those of the upper branch of the dispersion relation shown in Fig. S8 (i.e. $\sim 1170 - 1720$ Hz - note that the frequency in the plot is normalized by $\sqrt{k/m}$).

Movie S2 Experiment in which the impactor prescribes a displacement signal to the first square characterized by (u_1^{max}, v_1^{max})=(4.10 mm, 1166 mm/s). Note that after the pulse is applied the squares near the impactor vibrate at high frequency. This is because the applied impact results in a displacement signal that does not exactly match that of the supported solitary wave. Therefore, not all the energy applied by the impactor goes into the soliton and some activates vibrations of the squares near the impactor. It is important to note that these vibrations have frequencies in the range of those of the upper branch of the dispersion relation shown in Fig. S8 (i.e. $\sim 1170 - 1720$ Hz - note that the frequency in the plot is normalized by $\sqrt{k/m}$).

Movie S3 Experiment with the camera focused only on four squares, located at two-thirds of the sample. This experiment is conducted to capture the rotational waves propagating through the sample.

[1] J. A. Lewis, Adv. Funct. Mater. **16**, 2193 (2006).
[2] S. Shan, S. H. Kang, J. R. Raney, P. Wang, L. Fang, F. Candido, J. A. Lewis, and K. Bertoldi, Adv. Mater. **27**, 4296 (2015).
[3] J. R. Raney, N. Nadkarni, C. Daraio, D. M. Kochmann, J. A. Lewis, and K. B. Bertoldi, PNAS **113**, 9722 (2016).